LIVE CELL IMAGING

Optical computed tomography for spatially isotropic four-dimensional imaging of live single cells

Laimonas Kelbauskas, Rishabh Shetty, Bin Cao, Kuo-Chen Wang, Dean Smith, Hong Wang, Shi-Hui Chao, Sandhya Gangaraju, Brian Ashcroft, Margaret Kritzer, Honor Glenn, Roger H. Johnson, Deirdre R. Meldrum*

Quantitative three-dimensional (3D) computed tomography (CT) imaging of living single cells enables orientation-independent morphometric analysis of the intricacies of cellular physiology. Since its invention, x-ray CT has become indispensable in the clinic for diagnostic and prognostic purposes due to its quantitative absorption-based imaging in true 3D that allows objects of interest to be viewed and measured from any orientation. However, x-ray CT has not been useful at the level of single cells because there is insufficient contrast to form an image. Recently, optical CT has been developed successfully for fixed cells, but this technology called Cell-CT is incompatible with live-cell imaging due to the use of stains, such as hematoxylin, that are not compatible with cell viability. We present a novel development of optical CT for quantitative, multispectral functional 4D (three spatial + one spectral dimension) imaging of living single cells. The method applied to immune system cells offers truly isotropic 3D spatial resolution and enables time-resolved imaging studies of cells suspended in aqueous medium. Using live-cell optical CT, we found a heterogeneous response to mitochondrial fission inhibition in mouse macrophages and differential basal remodeling of small (0.1 to 1 fl) and large (1 to 20 fl) nuclear and mitochondrial structures on a 20- to 30-s time scale in human myelogenous leukemia cells. Because of its robust 3D measurement capabilities, live-cell optical CT represents a powerful new tool in the biomedical research field.

INTRODUCTION

Live-cell imaging has advanced significantly in terms of spatiotemporal resolution and multiplexing capabilities, enabling breakthroughs in our understanding of subcellular biomolecular processes. Important achievements such as spatial resolution beyond the diffraction limit (*1*–*5*) and high-speed/high-content imaging while minimizing phototoxicity (*2*–*4*) have propelled the field into the next cycle of application-driven developments for addressing cell biology questions that were previously unapproachable (*5*–*9*). Understanding the internal organization of a biological cell, inherently three-dimensional (3D), is pivotal for the next level of analysis of cellular function and response to external stimuli and stress (*10*–*14*). Quantitative characterization of cellular events in the context of the 3D structural framework of the cell is critical for achieving detailed insights into cellular functions in normal and diseased states (*15*–*17*).

A key prerequisite for performing inquiries into cellular architecture is the ability to image living cells in 3D with spatial resolution that is the same along the three spatial axes (isotropic). Despite the significant advances in 3D imaging of live cells, only a few methods offer nearly isotropic 3D spatial resolution (*4*, *18*, *19*). Furthermore, most of these imaging modalities require the cell to be immobilized during imaging, which may compromise biological dynamics when imaging natural suspension cells, for example, immune system cells. The cellular microenvironment is crucial for cell function, homeostasis, and pathogenesis (*20*, *21*). Consequently, studies focusing on the immune system, which rely on artificial immobilization of cells on substrates, may alter cellular organization and affect signaling pathways, because the natural state of these cells is in liquid suspension or nonadherent in tissues.

X-ray computed tomography (CT) has been the method of choice in the clinic for a broad variety of applications ranging from diagnostic to prognostic tests. The method offers truly isotropic spatial resolution (*22*), making it amenable to quantitative data analysis. X-ray CT relies on the collection of 2D projection images taken at varying angular orientations around the 3D object, allowing back-projection algorithms to reconstruct the original 3D object. Conventional optical quasi-3D imaging approaches such as confocal fluorescence microscopy rely on collecting 3D information of the cell with anisotropic, orientation-dependent spatial resolution [resolution along the optical (z) axis is about two times lower than that in the imaging (xy) plane] using multiple serial optical slices along the optical axis. Consequently, the resulting 3D image has significantly lower resolution along the z axis. In contrast, the optical CT approach is based on acquiring 2D images around a rotational axis where each 2D image has the same resolution. As a result, the spatial resolution of the reconstructed 3D volumetric image can approach isotropic resolution with sufficient sampling. Several studies have demonstrated the possibility to apply CT principles in the optical spectral range in absorption and fluorescence modes for imaging of fixed cells (*1*, *23*, *24*). Although powerful, the approach is limiting in terms of the ability to study real-time functional dynamic events in living cells. Applying the same principle for functional imaging of living cells using fluorescence would offer a significant advantage in the study of dynamic cellular events in homeostasis and in response to perturbations.

Adapting CT principles in the optical domain for live-cell imaging requires the cell to be rotated stably and continuously for acquiring angular projection images. In previous studies, the rotation of fixed cells was achieved by rotating microcapillaries containing cells embedded into a thixotropic index-matched gel inside of a hollow glass fiber (*24*). However, although the fixed cell capability enables a deeper understanding of cell pathology, the medium used in this case is highly cytotoxic and not amenable for live-cell studies.

We present a method based on CT principles for functional fluorescence imaging of live cells in suspension with isotropic 3D diffraction-limited spatial resolution. The method—live-cell CT (LCCT)—relies on

Center for Biosignatures Discovery Automation, The Biodesign Institute, Arizona State University, 1001 S. McAllister Avenue, Tempe, AZ 85287, USA.
*Corresponding author. Email: deirdre.meldrum@asu.edu

the acquisition of a series of 2D "pseudoprojection" (PP) images from different perspectives of the cell. The cell rotates around an axis that is perpendicular to the optical axis of the imaging system. This rotation orientation is important because it enables the 360° interrogation of the entire 3D structure of the cell using hundreds of 2D projection images to tomographically reconstruct the 3D cell.

We report the development of an experimental platform deploying the LCCT method. As a validation of the utility of the approach, we present the results of a study on mitochondrial and nuclear dynamics in immune system cells. Because of its capability to perform imaging of live suspended cells and the relative ease of implementation, we expect the LCCT method to become a powerful new tool for the biomedical research community.

RESULTS

Principle of optical CT of live cells

Similar to x-ray CT, optical CT in the visible spectral domain provides isotropic spatial resolution by reconstructing the 3D structure of an object from multiple 2D projection images acquired at different angular orientations of the object (Fig. 1A). However, there is a key difference between how data acquisition is performed in x-ray CT and in optical CT. The thin focal depth of high-resolution optical objective lenses is much smaller (typically, 0.5 to 1 μm) than the cell dimension (10- to 20-μm diameter), preventing the collection of 2D projection images by the same method used in x-ray CT where the point source and geometric ray paths form projection images without a lens. The focal-plane limitation can be overcome by collecting the fluorescence emission signal on the camera chip while rapidly scanning the objective lens along the optical (z) axis over a range that is large enough to interrogate the entire cell (Fig. 1B). As a result, emission signals emanating from the whole cell can be integrated by the camera chip (in time) during each of these scans, effectively producing a PP—the mathematical equivalent of a projection that one would obtain with a geometric beam (Fig. 1C) (*25*), except that a spatial, high-frequency band-pass filter should be used on each projection image to remove the accumulated low-frequency background. Cell rotation is accomplished by placing the cell inside of a 3D high-frequency electric field with a rotating spatial profile produced by an octupole of microelectrodes that are arranged symmetrically on two layers (Fig. 1D and fig. S1). The electric field creates a torque on the cell through interaction with the induced dipole moment in the cell. Typically, 300 to 500 projections are collected over a full rotation (360°) at an angular sampling rate of 1.2° to 0.72°, respectively. A volumetric (3D) image of the cell is then reconstructed using computational algorithms. The system setup is described in Materials and Methods.

Cell rotation

To achieve controllable and stable cell rotation, we developed an electrocage based on high-frequency electric fields with a rotating phase pattern in the 3D space. The cell rotation is a result of an induced dipole moment in the cell due to the rotation of the electric field that imposes a torque on the cell (*26*, *27*). In this case, the electric field plays a dual role. First, it provides a trapping force due to negative electrophoresis that pushes the cell toward the center of the electrocage where the electric field is minimal. Second, it generates a torque on the cell as a result of the induced dipole moment aligning along the orientation of the electric field in 3D. Although several other methods for cell rotation exist (*28*, *29*), we found that the electric field approach produced the most satisfying results in terms of stability, rotation speed, and minimal cell stress (see Materials and Methods). The rotating electric field pattern is generated by applying a sinusoidal waveform at a frequency of 1 to 2 MHz and peak-to-peak amplitude of 1 to 2 V to each of the microelectrodes with a phase offset by 90°. Using the electrocage, we are able to controllably rotate live myelogenous leukemia cells (K562 cell line) and mouse macrophages (J774A.1 cell line) at stable speeds ranging between 1 and 3 rpm (Fig. 2A and movie S1), during which time the camera can collect hundreds of 2D PP images around 360° to support 3D tomographic image reconstruction.

We characterized the rotation stability of cells by measuring lateral, in-plane shifts in the x and y directions during a full 360° rotation of the cell. We found that our approach yields reliable and smooth cell rotation (Fig. 2, B and C). Although the lateral displacement of cells varied from cell to cell, it appeared to depend on the cell shape (or how far it deviated from an ideal spherical shape). Image analysis revealed a coefficient of variation or relative lateral shift from the initial (0°) cell position of 0.057 and 0.084 of the cell diameter in the x and y directions per full rotation of the cell, respectively (Fig. 2B). We note, however, that these shifts take place over an entire rotation of the cell (20 to 60 s) and are relatively slow when compared with the time scale of an individual, one-direction half-cycle scan PP acquisition (40 ms). Consequently, adjusted to the 40-ms time scale, these shifts can be ignored, because they become minor, resulting in only about 10^{-4} shift of the cell diameter (assuming 2 rpm or 30 s per rotation; Materials and Methods), and do not distort PP images appreciably. As a result, lateral shifts on this time and spatial scale can be reliably corrected computationally using appropriate algorithms (Materials and Methods).

To fully characterize cell rotation stability, we determined how stable the rotation rate is over multiple rotations of the same cell. To this end, we calculated the coefficient of variation of the rotation rate using the data of five cells with five to seven full rotations each (Fig. 2C). We find that the average coefficient of variation of the rotation rate per full rotation is 0.051. Similar to the argument presented for the lateral shift, this results in 7×10^{-5} average variation in rotation rate per single PP and does not appreciably affect data collection (see Materials and Methods for calculation details). We note that for most of the studied cells (~95% of cells), the orientation of the rotation axis of the cell remained stable during rotation. Cells that exhibited slight but appreciable wobbling were excluded from analysis.

To further characterize the precision of the method of rotation, we studied the effects of varying electric field amplitude and frequency on cell rotation characteristics. We found an optimal range for the electric field amplitude and frequency to be 2 V (peak to peak) and 0.5 to 2 MHz, respectively (figs. S2 and S3). The amplitude range was selected on the basis of the number of successfully rotated cells (out of 10; fig. S2), whereas the frequency range was selected on the basis of the target cell rotation speed of 1.5 to 2 rpm and its relative insensitivity to the electric field frequency (fig. S3).

Imaging human myelogenous leukemia cells

After establishing reproducible and stable cell rotation, we performed a series of imaging experiments with live K562 cells with the goal of characterizing the spatial and temporal resolution of LCCT. To determine the spatial resolution, we used 200-nm-diameter fluorescent beads internalized through endocytosis into cells as a "biological" phantom. The beads were incubated with cells at low concentration so that each cell contained, on average, between 3 and 10 beads distributed sparsely inside the cell (fig. S4). The cells were then rotated and imaged in the electrocage under the same conditions as in a typical experiment (movie S2).

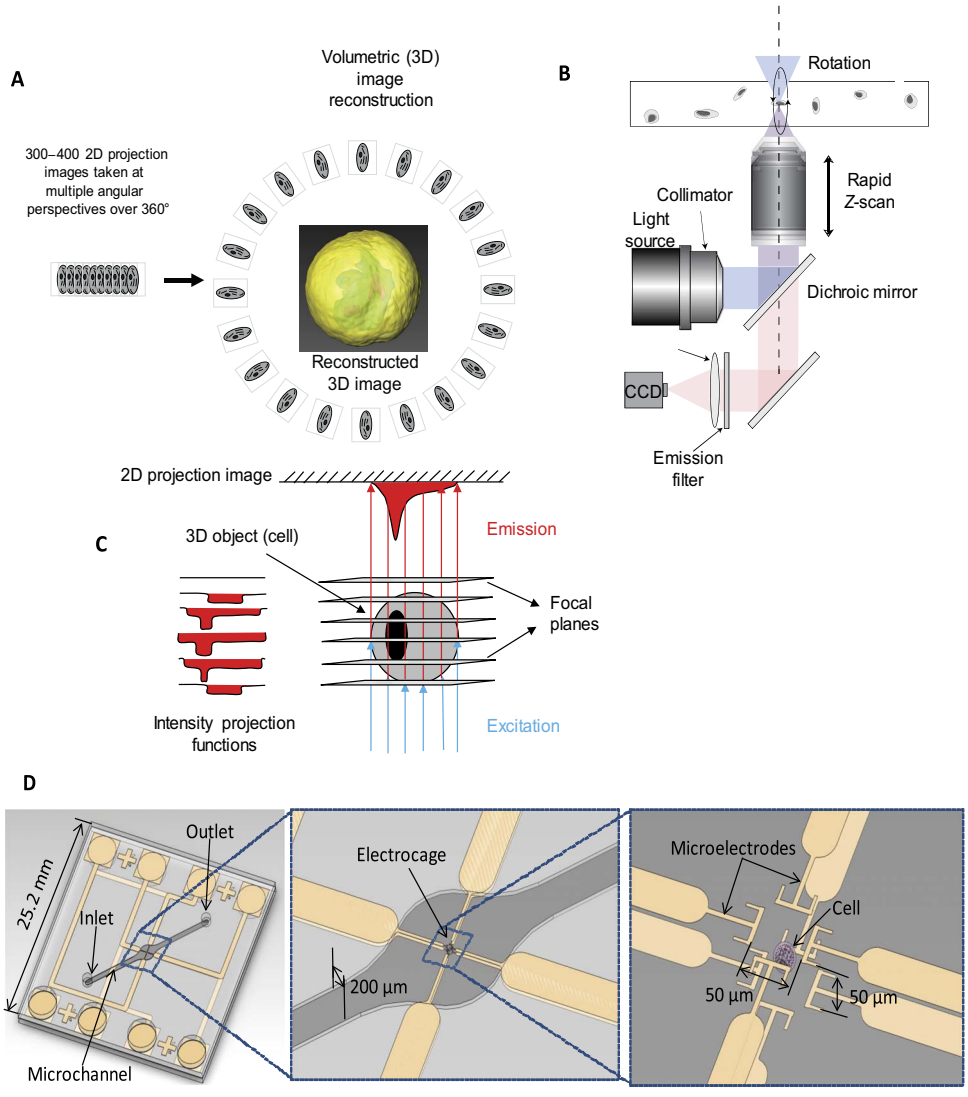

Fig. 1. Principle and experimental approach of optical CT. (**A**) Typically, 300 to 400 2D projection images at varying angular orientations of the cell are collected during a full 360° rotation perpendicular to the optical axis of the imaging system. The 3D volumetric image of the cell is computationally reconstructed using either classical [filtered back projection (FBP)] or algebraic (iterative) algorithms. (**B**) Setup of instrumentation for 2D projection acquisition. CCD, charge-coupled device. A high–numerical aperture (NA) objective lens is scanned along the optical (*z*) axis with an open camera shutter during a full scan in one direction resulting in a single image per scan (**C**). This mode of acquisition in the optical spectral range produces images equivalent to 2D projections in x-ray CT. (**D**) Microfabricated device for rotating live cells using high-frequency electric fields rotating in 3D space. The device comprises a fluidic channel for cell delivery and an octupole of microelectrodes for creating 3D spatially distributed electric field.

Reconstructed volumetric image data were used to characterize the point spread function (PSF) of the system (Fig. 2D and movie S3). We determined the spatial resolution as the full width at half maximum of the bead intensity profiles (Fig. 2, E and F). We found a resolution of 311 ± 20 nm in the planar direction (*xy*) and 266 ± 34 nm in the axial direction (*xz*). This corresponds closely with the theoretical limit of the spatial resolution due to a diffraction of 258 nm and is expressed as $d = 0.61\lambda/\mathrm{NA}$, where λ is the wavelength of the emitted light (550 nm in our case), and NA is the numerical aperture of the objective lens (1.3 in our experiments). The optical pixel size of the system is 107 nm, which satisfies the Nyquist sampling criterion of 258 nm/2 = 129 nm for diffraction-limited spatial resolution (Materials and Methods). We note that despite the about 10% difference in the spatial resolution along the two directions, the difference is within the measurement error.

Our approach of using point-like emission sources such as beads inside of live cells closely replicates real imaging conditions. This strategy accounts for refraction and scattering inside the cell in contrast to the widely used method of using fluorescent beads suspended in pure aqueous solution as a calibration standard (*30*, *31*). One of the most important factors in determining the spatial resolution of our approach is the number of projection images collected during one full rotation. The higher the number of projections, the denser the spatial sampling of the object, which translates into a more accurate representation of the spatial object's data.

It is important to note that there are several limiting factors determining the speed at which projection images can be collected. First, the number of fluorescence photons emitted by the fluorophore molecules over a unit of time (emission intensity) and, consequently, the

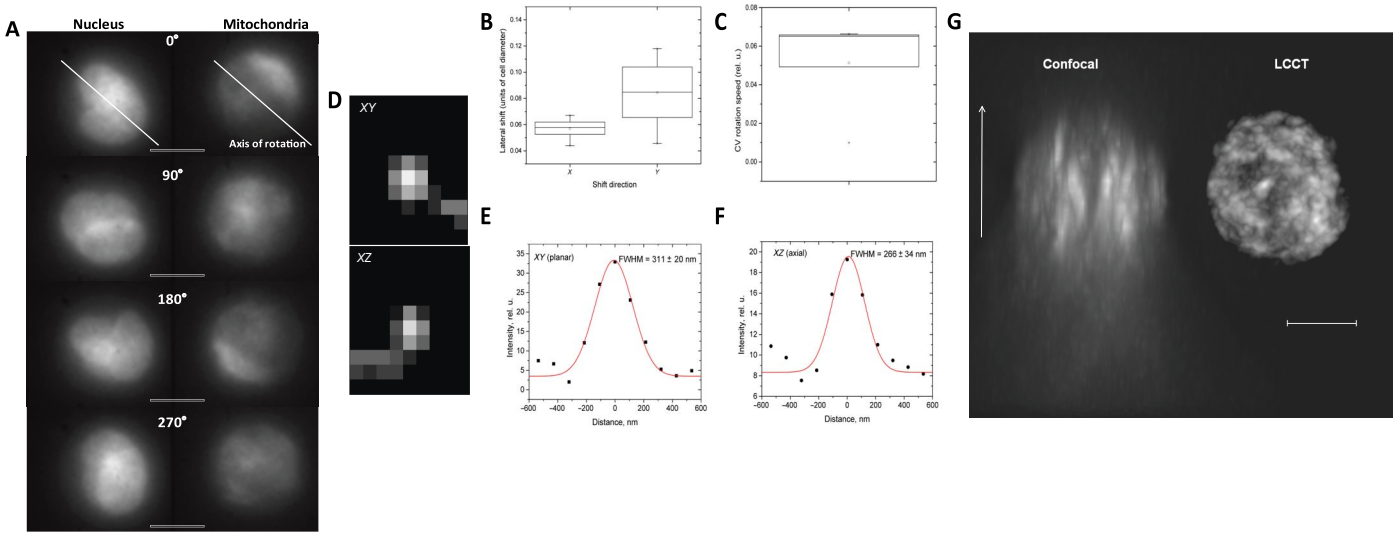

Fig. 2. Characterization of rotation stability and spatial resolution. (**A**) Projection images obtained at four orientations of the cell during a full rotation in the electrocage device. Scale bars, 5 μm. (**B**) Lateral shift of the cell along the *x* and *y* axes during one full rotation. Small relative planar average relative deviations were observed in both directions (0.057 and 0.084 of the total cell size in the *x* and *y* directions, respectively). (**C**) Rotation rate stability. The plot shows average coefficient of variation (CV) of rotation speed calculated using the data of five cells over five to seven rotations each. The box charts in (B) and (C) show the following statistical values: open square, mean; solid line, median; upper and lower box lines, 75th and 25th percentiles, respectively; upper and lower whiskers, 95th and 5th percentiles, respectively; x, maximal and minimal values. rel. u., relative units. (**D**) Spatial resolution characterization using 200-nm fluorescent beads. Beads were internalized by the cells before the experiment. Images of one such bead are shown in the *xy* and *xz* directions. (**E** and **F**) Analysis of axial (E) and lateral (F) spatial resolution. FWHM, full width at half maximum. (**G**) A comparison with confocal imaging reveals the advantage of the LCCT approach of distortion-free, orientation-independent 3D imaging due to isotropic spatial resolution. MIP renderings of the nucleus of the same reconstructed 3D image of a K562 cell using either a conventional confocal *Z*-stack or PP (LCCT) data are shown. The arrow indicates the orientation of the optical axis for confocal imaging. Scale bar, 5 μm.

signal-to-noise ratio (SNR) of the image play a major role. One can increase the emission photon intensity by increasing excitation light intensity at the expense of increased photobleaching rate. As a result, a balance between SNR and photobleaching needs to be established. We found that we could reliably acquire projection images with an SNR of 4 to 10, when collecting images at a rate of 10 frames/s without causing significant photobleaching for continuous imaging over 5 min using the Hoechst 33342 nuclear stain (fig. S5). Second, in our approach, the number of projections that could be collected during one full rotation was the scan speed of the objective lens (Fig. 1B). Because of the considerable weight of high-NA objective lenses (~300 g), inertia becomes a limiting factor by distorting the linear part of the scan at speeds markedly higher than 10 scans/s.

The temporal resolution of the approach was determined as the time needed to collect a full set (300 to 400) of projection images with high SNR to produce high-quality volumetric reconstructions. To this end, we stained the nucleus and mitochondria of K562 cells and collected projection images at rotation speeds of 1 to 3 rpm, which resulted in a temporal resolution of 60 to 20 s per volume, respectively. We note that we were able to achieve higher temporal resolution of down to ~7 s per volume by increasing the rotation speed and reducing the number of projections per rotation. However, the overall quality of the reconstructed volumes was reduced because of the smaller total number of projections per rotation, which resulted in lower SNR.

We compared 3D imaging capabilities of the LCCT approach with those of confocal imaging. To this end, we imaged the same cells with fluorescently labeled nuclear DNA using both imaging modalities, where we reconstructed 3D images of the nucleus from confocal *Z*-stacks or PP data in the case of LCCT (Fig. 2G and movie S4). As expected, we found that the typical elongation of the object along the optical axis of the system due to inferior spatial resolution in confocal imaging was absent in reconstructed 3D images obtained with LCCT due to isotropic spatial resolution. This illustrates the advantage of the LCCT approach to perform orientation-independent measurements of live cells with the same spatial resolution along all three spatial directions.

A representative example of reconstructed volumetric data of a live K562 cell with fluorescently stained nucleus and mitochondria is shown in Fig. 3. The nuclear stain revealed a highly varying pattern of DNA density distribution inside the nucleus presented as maximum intensity projection (MIP) images taken at three orthogonal orientations (Fig. 3A). Furthermore, the volume-rendering image (false-colored panel) shows surface textural features and a fold-like feature (Fig. 3A, arrow) with colocalized mitochondria (Fig. 3, C and D, and movie S5). Overall, the mitochondria of the cell appear distributed in a nonrandom manner around the nucleus.

We performed feature extraction based on the intensity histogram thresholding to demonstrate the ability to obtain quantitative information about nuclear and mitochondrial structural features. Figure 3 (E and F) depicts segmentations of the nuclear (movie S6) and mitochondrial (movies S7 and S8) features (colored overlays on MIP images) in the upper 30% of the intensity scale, correspondingly. The rather simple segmentation illustrates how quantitative 3D spatial information (center of mass coordinates, volumes, relative positions, etc.) about structural features can be extracted and analyzed. We note that although MIP images represent a good solution for presenting the 3D data in 2D format, there is an intrinsic limitation in that a substantial amount of intensity detail is lost, especially when presenting densely distributed small structures with varying intensity. To illustrate the appearance of the mitochondria more adequately, we show these organelles in the

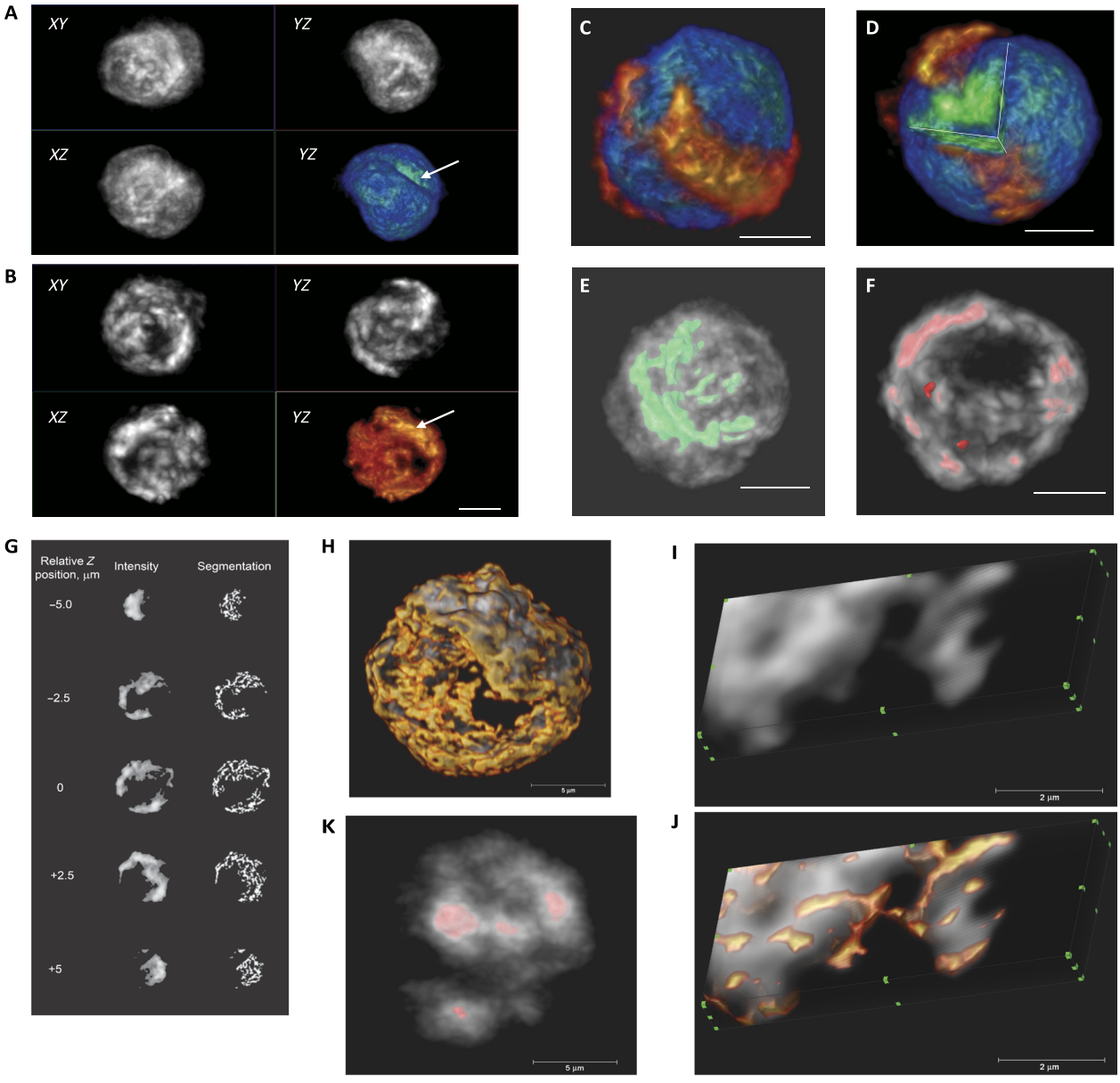

Fig. 3. Volumetric 3D reconstruction of the nucleus and mitochondria of a live human myelogenous leukemia cell (K562 cell line). (**A**) MIP images at three orthogonal orientations (grayscale) and volume rendering (color, lower right) of the nuclear DNA stained with Hoechst 33342. Lighter regions in the MIP images correspond to higher density of the DNA. A fold-like feature can be seen in the volume rendering (arrow). (**B**) The mitochondria of the same cell as in (A) stained with the mitochondrial marker MitoTracker Red. A volume rendering (lower right) indicates some of the mitochondria colocalized with the fold in the nucleus in (A). (**C**) Overlay of the volume renderings of the nuclear and mitochondrial data shows some of the mitochondria aligned with the fold in the nucleus in (A). (**D**) A cutaway presentation of the overlay reveals mitochondria located deep in the nuclear fold (movie S5). (**E** and **F**) Partial segmentation of the bright (70 to 100% range of the intensity histogram) nuclear and mitochondrial structures, respectively, using an intensity threshold above 70% of the camera detection dynamic range highlights the brightest features of the two organelles. The nucleus and mitochondrial data sets were acquired simultaneously. Both sets of data were deconvolved using a Gaussian PSF. Scale bars, 5 μm. (**G**) Reconstructed volumetric LCCT image of the mitochondria of the same cell presented as a series of slices through the cell at different depths (left). The contrast was enhanced in the intensity images to make less intense structures visible. The panel on the right shows segmentation of the mitochondria using the Niblack local threshold approach. The segmentation results were smoothed to enhance visibility. Scale bar, 5 μm. (**H**) 3D surface rendering of the mitochondrial network of the same cell with fluorescence intensity and segmented mitochondria shown in gray and orange, respectively (movies S11 and S12). (**I** and **J**) Mitochondrial fluorescence intensity (I; surface rendering) and the corresponding segmentation result (J) of a selected small region of interest (ROI) of the same cell. (**K**) 3D MIP image of the nucleoli of a live K562 cell. The nucleoli appear as bright clusters and were segmented (red structures) using an intensity threshold (movie S15). The diffuse fluorescence is a result of the nucleolar stain binding to RNA. The MIP image was deconvoluted and filtered using a Gaussian filter for increased clarity.

form of slices at five different depths of the reconstructed 3D image along with the corresponding segmentation results (Fig. 3, G to J, and movies S9 to S12).

It is possible that the mitochondrial dynamics during the collection of a full set of projection images (full cell rotation or 30 s) may lead to a blurred appearance of the mitochondria in volumetric images. To evaluate this aspect, we imaged mitochondria in fixed K562 cells using confocal microscopy (movies S13 and S14). In both cases, the mitochondrial morphology is qualitatively similar and appears as complex, dense 3D networks distributed around the nucleus.

To obtain a deeper insight into nuclear architecture, we further imaged the nucleoli in K562 cells (Fig. 3K and movie S15). As expected, we observed distinct high-intensity clusters representing the nucleoli inside the nucleus. The number of clusters per nucleus varied markedly from cell to cell, ranging from 3 to more than 10 in some cases, suggesting substantial heterogeneity in this cell type.

Nuclear and mitochondrial dynamic study

Mitochondrial fission inhibition

To validate our approach, we conducted a series of experiments where we compared mitochondrial distribution characteristics in untreated naïve mouse macrophages (J774A.1 cell line) with macrophages treated with an inhibitor of mitochondrial dynamics. We expected to observe an increase in the mitochondrial volume resulting from treatment with validated mitochondrial division (fission) inhibitors. We compared two different inhibitors, mdivi-1 (*32*) and 8–bromo–cAMP (cyclic adenosine monophosphate) (*33*), as they demonstrated large effects on mitochondrial dynamics. After conducting preliminary confocal imaging, we found that 8-bromo-cAMP exhibited the largest effect on mitochondrial distribution (fig. S6). We collected image data and performed mitochondrial morphology analysis of 30 untreated J774A.1 cells and 30 cells after treating them with 8-bromo-cAMP. A representative comparison of reconstructed 3D volumetric images is shown in Fig. 4A and movie S16. Because of isotropic spatial resolution offered by the method, we were able to calculate absolute volumes of mitochondrial clusters.

We developed a custom computational pipeline for processing reconstructed 3D images. The pipeline includes the background subtraction, contrast enhancement through intensity normalization steps, followed by adaptive local thresholding using the Niblack method (*34*), and a 3D object counting steps based on the nearest neighborhood connectivity. As expected, we observed marked alterations in the mitochondrial distribution, namely, the presence of large clusters as compared with the seemingly smaller, more diffusely distributed mitochondrial structures in untreated cells (Fig. 4, B and C). Not all cells exhibited these marked changes in mitochondrial distribution. After a close examination of all recorded data sets, it became clear that a portion of the treated cells exhibited less marked changes in the mitochondrial volume. A detailed analysis of the entire sample revealed a less pronounced but statistically significant increase in the average volume of mitochondrial structures after treatment (Fig. 4, D and E).

Although our developed image processing and feature extraction pipeline gave satisfactory results, we also know that it can be improved to better account for the interconnectivity between the mitochondria. Custom computational tools and optimized pipelines need to be developed to account for specific aspects of features such as joining, intensity variation, local noise patterns, etc. Improved feature extraction pipelines specifically tailored toward 3D volumetric imagery of cells in suspension would enable full utilization of the quantitative aspect of the approach.

Mitochondrial and nuclear dynamic studies

We next conducted a series of experiments in which we used the LCCT platform to explore intrinsic temporal characteristics of nuclear and mitochondrial morphology in mouse macrophages (J774A.1 cell line). For each cell, we acquired projection images over a time period of ~3 to 5 min during continuous rotation at a temporal resolution of 30 s. We acquired nuclear and mitochondrial morphology data for a total of 30 J774A.1 cells. The data analysis of the reconstructed 3D images was performed using a similar analysis pipeline as outlined in the mitochondrial fission inhibition study above. Briefly, the images were background-subtracted, and a local adaptive threshold was applied. Then, intensity normalization features were extracted using a 3D object counting routine based on the nearest neighborhood connectivity. Movie S17 shows a representative time-lapse 3D reconstruction of a J774A.1 cell. We extracted and calculated features for both the mitochondria and the nucleus. Because of isotropic spatial resolution provided by the LCCT method, we could determine a number of quantitative morphology characteristics, including feature volumes, positions of the centroids and center of mass with respect to the 3D volume, and mean densities. Figure 5 shows a typical data set of feature volume distribution over time for the cell shown in movie S17. In general, we observed that features in the lower range of volumes (0.1 to 1 fl) show markedly less temporal variation in volume as compared to the larger structures (1 to 20 fl).

DISCUSSION

We believe that this is the first report of immune system cells imaged in suspension with isotropic 3D spatial resolution. Furthermore, absolute volumetric data of nuclear and mitochondrial distribution and dynamics have been obtained with the LCCT. We note that many other commercial fluorophores can be used to target other organelles or proteins in live cells. Our experimental findings indicate that a majority of mitochondria in suspension cells are highly interconnected, forming a complex and dynamic filamentous network. The quantification of mitochondrial and nuclear remodeling over time enables direct multiparameter comparisons between individual cells or cell types, offering a unique way for rare cell identification with high accuracy. The quantitative data obtained with LCCT are amenable for multiparameter characterization of cellular phenotypes with improved sensitivity and specificity as compared to other, semiquantitative imaging modalities.

The isotropic 3D spatial resolution provided by LCCT enables absolute measurements at the diffraction limit. Spectrally resolved imaging permits simultaneous detection and correlation of structural and functional alterations in different organelles and/or regions of the cell. The number of spectral channels can be increased by spectrally splitting emission photons onto different quadrants of the detector or using additional detectors. Although here we present only a limited number of morphometric nuclear and mitochondrial features, the set of quantitative features can be expanded markedly by adding a variety of established textural measures to the computational quantification pipeline (*35*). This would not only increase the amount of detail obtainable on a single-cell basis but may also substantially improve statistical power of differentiating cell subtypes. Although the current spatial resolution of the method is diffraction-limited, it is conceivable that some of the advanced super-resolution imaging modalities may be combined to surpass the diffraction limit. Modalities based on single emitter localization [stochastic optical reconstruction microscopy (STORM) and photoactivated localization microscopy (PALM)] or stimulated emission depletion via engineered PSF (*36*) may be too slow for imaging of densely stained entire cells

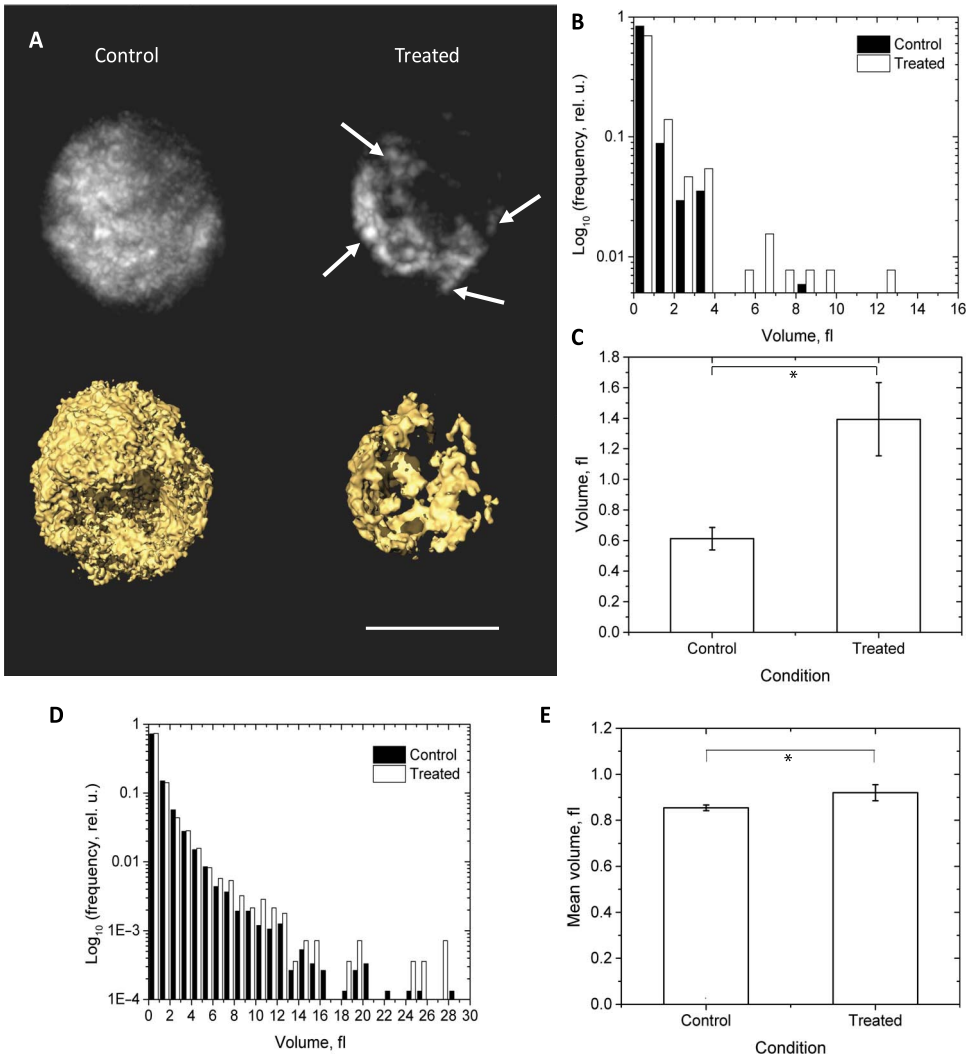

Fig. 4. Biological validation study using the mitochondrial fission inhibitor 8-bromo-cAMP in mouse macrophage J774A.1 cells. As expected, larger mitochondrial structures (bright spots, arrows) were observed as a result of mitochondrial fission inhibition. (**A**) Comparison of an untreated J774A.1 cell (left) and one treated with 8-bromo-cAMP (right). MIP (top row) and isosurface rendering (bottom row) show a marked shift toward larger structures. (**B**) Quantitative analysis of the mitochondrial structure volumes corroborates the qualitative findings of (A) showing the appearance of structures with larger volume in the treated cell. (**C**) A comparison of the average values of the volume distribution demonstrates statistically significant ($P = 0.001$, Kolmogorov-Smirnov test) increase in the volume of the structures after treatment. (**D**) Combined mitochondrial structure volume distribution of 30 control and 30 treated cells. A trend toward increasing volume of the structures can be seen. (**E**) The average values of the volume distribution show less pronounced but statistically significant ($P = 0.008$, Kolmogorov-Smirnov test) increase in the mitochondrial volume in treated versus control cells.

and/or damaging to make such a combination biologically reasonable. On the other hand, modalities such as structured illumination microscopy (SIM) (*37*, *38*) or image scanning microscopy (ISM) (*25*), which both offer about twofold increase in spatial resolution, appear as feasible candidates. Because of their wide-field image acquisition mode, which is directly compatible with LCCT, both SIM and ISM could be used to acquire projection images with a resulting isotropic resolution of 125 to 150 nm.

We note that the mitochondria of the suspended cells (Figs. 3 and 4) appear different from what one would typically expect from confocal imaging of the mitochondria in cells adhered to a planar substrate. In adherent cells with most of the mitochondria located in a flattened thin layer of the cytoplasm, one can usually observe individual mitochondria in the shape of elongated string-shaped or round structures (fig. S6). Contrary to separate mitochondria, mitochondria in our images appear distributed around the nucleus and form a complex, dense 3D network partially in the form of clusters of varying sizes. It is possible that this appearance of the mitochondria is due to three not mutually exclusive causes: (i) mitochondria movement during imaging, (ii) cell type specificity, and/or (iii) imaging immune system cells in their natural conformation—suspension—as opposed to adhered to a planar substrate. Our confocal images of the mitochondria in fixed K562 cells revealed a qualitatively similar appearance to the mitochondria in live cells (movies S13 and S14), suggesting that mitochondrial movement on the time scale of 30 s or less in the two studied cell types may be considered as a relatively minor factor in LCCT imaging. We therefore conclude that the observed mitochondrial morphology can be attributed to the cell type specificity and/or the fact that the cells are imaged suspended in 3D space rather than adhered on a planar substrate.

We demonstrated a temporal resolution of our method of ~30 s (time needed to acquire a full set of 2D projections of the cell), which

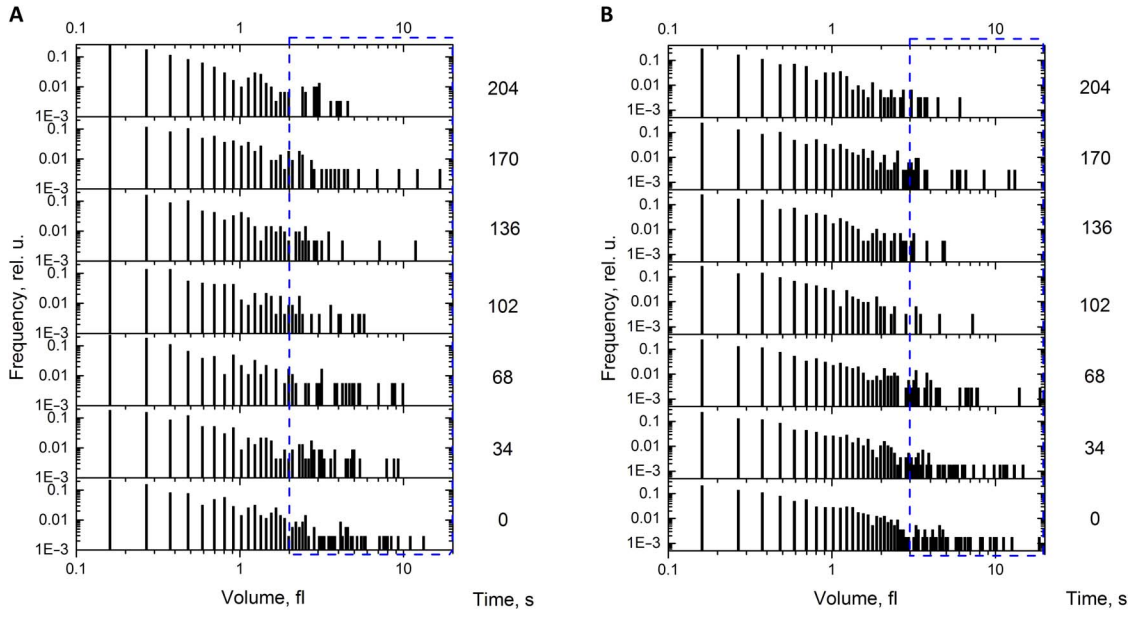

Fig. 5. Mitochondrial and nuclear DNA dynamic studies. Time-lapse data over 4 to 5 min of one J774A.1 cell were acquired, reconstructed, and segmented, followed by feature volume calculation. (**A**) Alterations in the nuclear DNA structure spatial distribution. The graph shows changes in the structure volume distribution over time, revealing most dynamics in the structures with larger volumes (2 to 12 fl, dashed rectangle), whereas the smaller features show little change. (**B**) Mitochondrial structure volume dynamics showed qualitatively similar behavior as the nucleus. Most of the changes can be seen in the structures with larger volumes (3 to 20 fl; dashed rectangle), whereas the smaller structures show relatively little alteration. The stacked graphs in each panel represent spatial distribution at a particular time point, as indicated to the right of each graph.

is mainly limited by the speed of scanning the objective lens. It is conceivable that cellular events taking place on a second scale, for example, mitochondrial fusion and fission, are detected as temporal averages resulting in blurring of the rapidly altering structures. Faster, resonant scanner systems can be used to increase the scan speed fivefold or more, resulting in improved temporal resolution. Depending on the properties of the fluorescent label, photobleaching and the resulting phototoxicity may become a limiting factor for time-lapse imaging experiments. Different illumination schemes, such as selective plane illumination (*2*) or HiLo (*39*), may be integrated into our system to alleviate the issue of photobleaching and increase imaging contrast.

In summary, the LCCT is a powerful and versatile tool for investigating cellular dynamics in cell suspensions in a quantitative fashion by enabling measurements in 3D space with diffraction-limited spatial resolution. The LCCT enables quantitative studies of cellular architecture dynamics and could be used for combined nuclear and mitochondrial organization studies in response to treatment.

MATERIALS AND METHODS

Electrocage microfabrication

The fabrication of the electrorotation chip required the bonding of two separate chips (180 and 500 μm thick), with four electrodes each, to form an octupole for cell rotation. A schematic of the standard cleaning, deposition, and photolithography procedures is shown in fig. S1.

Following the fabrication of the individual dies, the final chip for cell rotation was assembled. The 180-μm die with the micropatterned fluidic channel was used as the bottom half of the chip for imaging with high spatial resolution. The two dies were aligned on a mask aligner stage for precision control and were bonded by wicking in an ultraviolet (UV) adhesive via capillary forces. Once the microchannel has been completely surrounded by the UV adhesive, it was cured under UV light, which creates a permanent seal around the perimeter of the chip.

The electrical connections to the waveform generator were made on a custom printed circuit board with preexisting contacts. This approach enables convenient handling of the electrocage chip, which sits snugly on this fixture during experiments. There are two fluidic connections. A fluidic probe connected to a 50-μl syringe for precise manual control of fluid in the chip created a removable, sealed contact with one port of the microfluidic channel on the chip. A pipette tip or nanoport was glued to the other fluidic port and provided an inlet for introducing cells.

Cell culture and fluorescence staining

K562 cells (human chronic myelogenous leukemia cells) were cultured in RPMI 1640 medium (Gibco) containing 10% fetal bovine serum (Gibco), penicillin (100 U/ml), and streptomycin (100 μg/ml) at 37°C in a humidified incubator containing 5% CO_2. The cell density was determined using a Countess II FL Automated Cell Counter (Life Technologies). Cultures were maintained by the addition or replacement of fresh medium. J774A.1 cells (mouse macrophage cells) were cultured in Dulbecco's modified Eagle's medium supplemented with 10% fetal bovine serum (Gibco), penicillin (100 U/ml), and streptomycin (100 μg/ml) at 37°C in a humidified incubator containing 5% CO_2. Subcultures were prepared by scraping a 75-cm^2 flask, removing all but 10 ml of the culture medium. The volume was adjusted accordingly for different culture vessels. The cell density was determined using the automated cell counter. The nucleus and mitochondria of the K562 and J774A.1 cells were stained simultaneously using Hoechst 33342 (H3570, Life Technologies) and MitoTracker Red (M-7512). For staining, 3 μl of 0.5 μM Hoechst 33342 and 3 μl of 1 μM MitoTracker Red into a 1- ml 1 million cell sample were added and incubated for 30 min. The nucleoli in K562 cells were stained using the Nucleolar-ID Green fluorescent

marker (ENZ-51009, Enzo Life Sciences). For staining, 1 µl of the marker stock solution was added to 1 ml of cell culture medium containing 10^6 cells and incubated for 30 min at 37°C in a humidified incubator containing 5% CO_2. Before imaging, cells were spun down and resuspended in 1 ml of fresh cell culture medium.

Live cells with beads samples

To characterize spatial resolution of the system, we combined 200-nm-diameter beads (Life Technologies) with live K562 cells and imaged the cells with LCCT. To make the live cell and bead sample, 1 ml of cell medium containing 10^6 K562 cells was put into a polymerase chain reaction tube and mixed with 0.3 µl of bead stock. The sample was incubated for 4 hours to make sure that the beads were taken up by the cells. After 4 hours, the sample was centrifuged at 500*g* for 7 min to form a pellet, the supernatant was aspirated, and the pellet was resuspended in 1 ml of fresh cell culture medium. The centrifugation step was repeated twice to remove any remaining free beads in the medium.

Effects of electrocage parameters on cell rotation rate

The magnitude of the dielectrophoretic force is proportional to the gradient of the electric field, which is generated by the voltage applied to the microelectrodes. Therefore, it was important to ascertain that an appropriate starting voltage is chosen for experiments. The experiments were set up with a frequency fixed at 2 MHz and were done on a chip with a 50-µm spacing between the two electrode layers. The diameter of the tested human myelogenous leukemia cells (K562 cell line) was 18 ± 3 µm. A graph of the number of K562 cells successfully rotated as a function of voltage applied is shown in fig. S2. On the basis of this result, we chose the amplitude value of 2 V (peak to peak) as a good starting point to perform electrorotation.

The frequency of the electric field is closely related to rotational parameters like speed and rotational direction. To determine the relation between different frequencies and the cell rotation rate, the voltage amplitude was fixed at 2 V, whereas the frequency was adjusted from 0.2 to 7 MHz (fig. S3). The cell size and chip electrode gap were the same as for the previous voltage amplitude study. As expected, we observed an increase in the rotation rate with increasing electric field frequency. A slow rotation rate of 1 to 2 rpm was desirable for collecting a large number of PPs during one full rotation of the cell. The number of collected PP images directly affects the spatial resolution and SNR of the reconstructed volumetric images. Therefore, a working frequency range of 0.5 to 2 MHz was chosen as best suited for imaging. Lower frequencies were avoided because they may induce ionic currents leading to cell stress and membrane electroporation, although we observed that higher frequencies can lead to cell membrane damage.

Lateral movement and cell rotation speed calculation

The lateral shift in the *x* and *y* directions and rotation speed were determined as described previously (*28*). Briefly, the lateral shift was calculated from projection images taken during a full rotation of the cell. The cells were first segmented using an edge detection method, followed by removal of occasional small objects by applying a size exclusion filter. Finally, the geometric center coordinates of the cell in each image were calculated, and the lateral displacement of the cells in the *x* and *y* directions was determined by tracking the center position of the segmented cell.

The cell rotation speed was determined using the average gray level of a chosen ROI inside the cell over a full rotation as a measure of cell rotation period. In this case, the rotation of a cell was represented as a periodic pattern of the average gray value of the chosen ROI as a function of time. The rotation speed in rotations per minute was calculated as the inverse of time between two adjacent maxima or, in case of multiple rotations, by calculating the power spectrum of the curve and taking the highest frequency peak as rotation rate.

Rotational stability characterization

We observed two types of distortions of an ideal rotation in the electrocage that can affect the quality of 3D image reconstruction from 2D PP images: (i) lateral shift in the *xy* plane of the cell and (ii) alterations in rotation rate. We determined the average lateral shifts along the *x* and *y* axes during a full rotation of the cell to be 0.057 and 0.084 in units of cell diameter, respectively. Assuming a 10-µm-diameter typical cell, the average lateral shifts were 0.57 and 0.84 µm per full rotation of the cell. Our typical rotation rates were in the range of 1 to 3 rpm or 20 to 60 s per rotation. We calculate the average lateral shift per each individual PP as follows

$$s_{ave} = S_{ave} \times \frac{t_{exp}}{T_{rot}} \quad (1)$$

where S_{ave} is the average lateral shift along one axis per full rotation, t_{exp} is the exposure time for individual PP image acquisition, and T_{rot} is the rotation period. Assuming a 30-s rotation period and given the average lateral shifts along the *x* and *y* axes of 0.57 and 0.84 µm, respectively, and the exposure time of 40 ms, we calculate s_{ave} values of 0.76 and 1.12 nm for the *x* and *y* axes, respectively.

Our cell stability measurement yielded an average rotation rate instability of 5.1% per full rotation (Fig. 2C, open square). Assuming a typical rotation rate of 2 rpm (30-s rotation period), this translated into an absolute average instability of 0.1 rpm per full rotation. By analogy with the lateral shift calculation consideration, we define the average rotational rate error per individual PP using the following equation

$$r_{ave} = R_{ave} \times \frac{t_{exp}}{T_{rot}} \quad (2)$$

where R_{ave} is the average deviation of the rotation rate in revolutions per minute, t_{exp} is the exposure time for individual PP image acquisition, and T_{rot} is the rotation period. Given t_{exp} = 0.04 s and R_{ave} = 0.1 rpm and assuming T_{rot} = 30 s, we calculate a rotation rate instability per PP r_{ave} = 0.00013 rpm. We note that both types of instabilities—lateral shift and rotation rate instability—are small and do not affect the image quality of PPs appreciably in terms of introducing movement artifacts.

In addition to the deviations in lateral position and rotation rate of the cell, it is important to consider the fact that the cell rotates continuously during PP acquisition. Consequently, one needs to determine the amount of blurring that will occur because of the cell movement and how it may affect image quality. To this end, we determined the upper limit of this distortion by calculating the distance that a pixel at the outer boundary of the cell would travel during the exposure time over which a PP image is acquired. Using the same assumptions as above, that is, 10-µm cell diameter and 30-s rotation period (360° rotation), we calculate the angular distance of the cell during the 0.04-s exposure time for image acquisition as

$$\alpha = 360 \times \frac{t_{exp}}{T_{rot}} = 360 \times \frac{0.04}{30} = 0.48^\circ \quad (3)$$

The distance that a pixel at the outer boundary of a 10-μm-diameter cell would travel is the arc length

$$l = 2\pi r\frac{\alpha}{360} = 6.28 \times 5 \times \frac{0.48}{360} = 0.042\ \mu m = 42\ nm \quad (4)$$

where r is the cell radius. We can see that the motion blur is small compared with the spatial resolution of the system (280 to 290 nm at 550 nm) and can be neglected.

Assessment of cell stress in high-frequency electric fields

To assess the potentially adverse effects of exposure to a high-frequency electric field on cell health, we performed a series of experiments to assess cell stress. It is possible that the external electric fields generated by the electrocage may induce a stress response that manifests in changes in the biomolecular profile and/or alterations in the morphology of the cell. To address this question, we first designed and implemented a test platform to evaluate the stress at the bulk sample level (fig. S7). We used the well-understood electrical properties of a set of parallel electrodes that produce a uniform electric field $E = V/d$, where V is the voltage difference between the electrodes, and d is the separation between them. When the size of the electrodes is significantly larger than d, the electric field leakage at the edges was negligible. The device was composed of two 2″ × 3″ glass microscope slides with gold coating on one side and a 50-μm-thick spacer made of adhesive nonconducting tape used in the semiconductor industry. The separation between the electrodes was the same as that in the electrocage. After cells suspended in growth medium are pipetted onto one of the electrodes, the medium was sandwiched with a second electrode, and a voltage of 2 V at 2 MHz was applied across the electrodes. We selected the same alternating current waveform as that used in the electrocage, so the electrical stress between the plate electrodes can effectively simulate the actual situation during the cell rotation process in the electrocage. The presence of cellular stress was tested under five different conditions followed by Western blot analysis to monitor expression levels of the heat shock protein 70 (HSP70). We chose HSP70 as the stress indicator owing to its central role in the cellular stress response and high sensitivity to a broad variety of stress types (*40*–*42*). For each stress condition, we loaded approximately 2 million cells into the uniform electric field. A total of five conditions were tested. Condition 1 (control): Cells were kept in the incubator with no disturbance. Condition 2: Cells sandwiched between electrodes with no electric field were applied. This condition was tested to ensure that there is no significant stress caused by transferring cells onto the device. Condition 3: Cells between electrodes with the electric field were applied. Condition 4: Same as in condition 3, followed by a recovery phase at 37°C for 4 hours. Condition 5: Conventional heat shock at 42°C for 10 min as a positive control.

We found no significant increase in HSP70 expression levels resulting from the exposure to the electric field (fig. S8). In addition to the HSP70 expression levels, we performed time-lapse imaging of live K562 cells where we investigated whether a prolonged continuous exposure (>4 min) to electric field would induce measurable changes in cellular morphology. In line with the HSP70 findings, the imaging revealed no gross changes in cell morphology (cell size and overall intracellular organization) at submicrometer resolution during a continuous 4- to 5-min rotation in the electrocage (fig. S9). Furthermore, turning the electric field on or off in the electrocage did not cause measurable changes in cellular morphology. These findings suggest that the electric fields used for cell rotation in the electrocage do not cause measurable stress levels in live cells under experimental conditions used for imaging.

LCCT system setup

One of our main goals was to design an LCCT system simple enough to be replicated and implemented in any research or clinical laboratory. Therefore, the LCCT was designed around a standard, commercially available inverted microscope with epifluorescence imaging capability. A schematic of the LCCT system is shown in fig. S10A, and a picture of the complete system setup is shown in fig. S10B. We note that except for the microfluidic chip for cell rotation, all other parts are commercially available with some of them, such as the light-emitting diode (LED) light source and CCD camera, already in routine use by many laboratories worldwide. The system comprises three main subsystems: (i) cell rotation system, (ii) epifluorescence image acquisition system, and (iii) optional confocal optical imaging system for comparison purposes.

The cell rotation subsystem (fig. S10A) is composed of an integrated microfluidic chip (electrocage) that combines a microfluidic channel and eight microelectrodes arranged on two layers. An eight-channel computer-controlled waveform generator was used to create sinusoidal waveforms to drive the electrocage.

The image acquisition subsystem comprises an inverted microscope equipped with appropriate filters for fluorescence detection and an LED light source connected to the back port of the microscope for fluorescence excitation. A fast-scan piezo stage with an objective lens mounted on it was used to sweep the imaging plane of the objective lens through the entire cell for obtaining projection images. A dual-channel spectral module (DCSM) was attached to the right port of the microscope to split the emission photons coming from two different fluorophores into respective halves of the detector chip. Fluorescence was detected by a cooled electron-multiplying CCD (EMCCD) camera. Custom software was developed to control timing and synchronization between the cell rotation and imaging modules.

For comparison with and validation against another already established imaging modality, we integrated a commercial confocal swept-field module onto the left port of the microscope. This capability, although important in the device development and validation, is optional for routine CT imaging.

The LCCT system setup was built around a commercial inverted microscope (Ti-U, Nikon) equipped with a xenon arc lamp (wavelength range, 320 to 700 nm; Lambda LS, Sutter Instrument) or a multi-LED light source connected to the back port of the microscope for fluorescence excitation. A filter cube mounted in the microscope turret contained an excitation filter (FF01-407/494/576-25, Semrock) and a multichroic beam splitter (FF436/514/604-Di01-25x36, Semrock) for selecting appropriate excitation wavelengths that are absorbed by the fluorophore and blocks other sources of light. A fast-scan piezo stage (part of the confocal swept-field module described below) with an objective lens (S Fluor; 100× oil; NA, 0.5 to 1.3; Nikon) mounted on it was used to scan the image plane of the objective lens. An intermediate 1.5× lens mounted inside of the microscope was used to obtain a total optical magnification of ×150 (100× objective lens × 1.5× intermediate lens). A DCSM (DV2, Photometrics) was placed on the right port of the microscope to spectrally split the emission photons coming from two different fluorophores into respective halves of the detector chip. Each spectral channel was projected simultaneously onto one-half of a camera chip using two emission filters [FF01-452/45-25 (Semrock) and ET630/75m (Chroma Technology)] mounted in the DCSM. A cooled EMCCD camera (Evolve 512, Photometrics) was connected to the DCSM and

was used to acquire projection images. The physical pixel size of the camera was 16 μm × 16 μm, resulting in an optical pixel size of 16 μm/×150 magnification = 0.107 μm (107 nm). The optical pixel size was below the Nyquist criterion for diffraction-limited resolution of 258 nm/2 = 179 nm (assuming an emission wavelength of 550 nm and an NA of 1.3) and thus satisfied the spatial sampling requirement. An optional swept-field confocal (SFC) module (Prairie SFC, Bruker) was attached onto the left port of the microscope for comparison purposes. The SFC was equipped with four lasers with excitation wavelengths of 406, 488, 532, and 561 nm. The confocal image acquisition was accomplished using PrairieView v.5 software.

A critical part of the imaging subsystem was the acquisition hardware's integration and synchronization software. A custom LabVIEW (version 2015, National Instruments) program was written to trigger and synchronize the piezo stage with the camera. This software was needed to ensure that all required imaging and acquisition tasks are carried out in the proper sequence and with the proper timing and synchronization (fig. S11). This required software was realized with a suite of custom-designed independent software modules that are integrated with each other via software and electronic messaging. This approach ensures the utmost flexibility and robustness, as future development ensues. The significant functionality that this software must provide includes but is not limited to the following: precise timing and triggering of system image acquisition hardware (for example, camera exposure); precise timing and triggering of system fluorescence illumination (for example, LED control); precise timing and synchronization of cell rotation hardware (for example, electrocage); configuration and control of amplitude, frequency, and phase for the electrocage octupole; precise timing and synchronization of piezo-actuated objective (for example, the "piezo controller"); and control and automation of ancillary imaging hardware (for example, stage controllers).

An issue of particular importance with this portion of the software was proper timing and synchronization of the imaging acquisition hardware with the piezo controller. This is so critical because of the manner in which the projection data are acquired. To gather proper projection data, the start and stop exposure time of the image acquisition hardware must be precisely synchronized with the piezo controller to ensure that optical data are only collected at the proper time during the sweep of the objective through the imaging volume that encompasses the cell of interest (fig. S12). If projection data acquisition is not initiated and terminated at the optimal time during the sweep of the objective lens, then the data will either be lost or will be acquired during a nonlinear portion of the objective's sweep, causing distortion. In either case, degradation in the 3D image reconstruction will result. To achieve the desired image fidelity, with the stated temporal resolution and sample rate, the tolerance for error during this part of the hardware/software synchronization process was on the order of microseconds. This was achieved through a combination of electronic and software intermodule messages exchanged between the relevant modules (fig. S11). This approach to system-level abstraction and design allows for simultaneous and independent development of both imaging and cell delivery sections of the system, without either adversely affecting the other.

Image processing and reconstruction

Background correction

Using standard microscopy techniques to remove the background of these images was complicated by the motion of objective during acquisition. In addition to the standard problems of microscopy such as nonuniform illumination and variation in pixel sensitivity, there were the additional problems of fluorescing debris that sometimes appears in the field of view and uneven illumination intensity. We used the standard method within the fluorescence microscopy community for dealing with the uneven illumination, which is to acquire a series of images, although there is no sample in the field of view. These images were then averaged to produce a smooth background image without read noise from the camera and subtracted from raw data images.

Marker-free registration

The alignment and registration of the cells is the most important step for creating a quality reconstruction. During rotation, cell shape irregularities may cause the center of rotation to deviate slightly in unpredictable ways. Although these distortions can be corrected computationally, there are no usable fiducial marks within these cells, so the registration and alignment must be performed with only the information available from the cell. For registration, the motion of the cell was followed through all the projections by the judicial use of the center of gravity (COG) and watershed algorithms. This sequential procedure was necessary due to the axial and lateral motions of the cell. Occasional debris and other cells were masked from the calculation by using the watershed method to define the cell location. This procedure results in a good alignment of the cells, but there are jitter and misalignments that occur from the noise and irregularly shaped cells. This alignment procedure was acceptable to within the range of a few pixels. To produce high-quality reconstructions, the alignment must be further refined. The following are the techniques used in this study: COG, noised COG (nCOG), masked COG (mCOG), cross-correlation (CC), and template-matched CC (tmCC). CC and COG are well known and commonly used techniques. The nCOG adds a coherent noise known as the "jitter filter" to each projection and performs the COG method on each PP multiple times. Tuning the noise amplitude to the level of the systematic noise helped prevent the acquisition noise from causing jitter. mCOG performed an adaptive thresholding operation to produce a mask of the already found cell, and then, a feathering operation was performed on the mask to limit the effect of noise and debris on the final registration, before aligning the cell with COG. tmCC was performed by taking the roughly aligned PPs and performing a low-quality reconstruction of the data. The forward projections from this pseudoreconstruction were then used as templates to do the final alignment of the PPs by CC.

In the absence of a useful phantom, evaluation of the quality of the registration must be taken from the data itself. The quality of the registration techniques was rated following the methods described by Cheddad *et al.* (*43*), where the registered image is correlated with its mirror image taken at the opposite angle to give an idea of the correctness of the registration. The results in fig. S13 show that nCOG and tmCC performed better than the other methods, with nCOG being a much faster technique due to its simplicity. The technique helped to remove the distractions of stray noise and illumination. However, in the case of a cell that is imaged at a low SNR ratio or in the presence of debris near the cell, the tmCC method markedly outperforms the other methods.

Volumetric reconstruction of projection data

Reconstructions of LCCT projection data were computationally simpler than most tomographic reconstruction methods. The LCCT projection can be best approximated as a series of pencil (parallel) beams, as opposed to fan beams in conventional CT, extending from each camera pixel and rotating in a cylinder around the rotation axis. This geometry lends itself to a few high-performance algorithms.

On the basis of these considerations, a highly optimized algorithm has been developed to markedly reduce the computational time required for reconstructions. The speedup was achieved by structuring the code based on rays extending from the voxels in the reconstruction volume, instead of the conventional method of working from rays extending from the projection. This change in the perspective of the algorithm greatly reduced the number of calculations that must be performed to determine which voxel is affected by each ray. The second greatest cost for the reconstruction algorithm was in the interpolation of the ray's path through a voxel, thereby determining the weighting of the rays' effect on that voxel. Because these calculations can be computationally expensive, the interpolations were performed once for just one row of the whole volume. Once the weighting set was calculated, the weights could be used for all the rows in the PPs. This means that the interpolations were performed only once per projection instead of once per voxel. This computation can reduce the time of the calculation by two to three times. Last, the code has been optimized to run within OpenCL, allowing the code to be run on either a graphical processing unit or in a multiprocessor environment.

A variety of reconstruction methods were tested to determine which could produce the best result in terms of reconstruction quality and speed. These techniques include FBP, simultaneous iterative reconstruction technique (SIRT), Markov random field regularized reconstruction (MRF-RR), Tikhonov regularized SIRT (TV regularized SIRT), and online blind deconvolution reconstruction. Each method was tested against a number of standards. The advantage of the optical system was that the cell can be optically sectioned, giving a built-in phantom for the reconstruction. The optical section is of fairly low quality, so care must be taken in the comparison of the reconstruction and the volume. A few metrics have been developed and tested against human intuition to evaluate the quality of the reconstructions. Finally, all the reconstructions have been evaluated against a simulated cell phantom.

We performed the parallel beam FBP using the techniques outlined by Herman *et al.* (*44*). The projections were conditioned as described above by first subtracting the microscope background and correcting the overall intensity. Finally, we reconstructed the 3D volume using a Hann filter and bilinear interpolation. Blind deconvolution of the projections offers a number of advantages for iterative reconstruction methods. Within the framework of SIRT, instead of first completely deconvolving all the PPs and then back-projecting, the forward- and back-projection processes become part of each deconvolution iteration, allowing the determination of successively improved estimates, x'_{pp}, leveraging information available from the projection set as a whole. The breakdown of the technique is as follows (fig. S14):

For each projection angle over 180°,

1) Estimate initial x'_{pp} and f'_{pp} by using the acquired projection (y_{pp}) and its mirror twin (180° pair of parallel projections).

2) Perform SIRT to create a crude reconstruction using all acquired projections (current 3D image estimate V').

3) Forward-project V' to get x'_{pp} and use this image to provide the current estimate for the deconvolution. Refine f'_{pp} and x'_{pp} using the regularization technique (Markov random field, Tikhonov, total variation, or blind deconvolution) for several iterations using the y_{pp} and its mirror (180°) twin. The additional benefit of this operation is that the x'_{pp} alignment is refined on each iteration.

4) Back-project the difference (error function) between the current forward projection and x'_{pp}.

5) Repeat steps 3 and 4 until a stop condition is reached.

This method was more computationally expensive than standard SIRT methods, but the simplicity of the pencil beam projection made it reasonable. The cost must be balanced carefully by pre-estimation of the reconstruction and PSF for each projection. As shown in fig. S15, our SIRT technique resulted in a finer-grained reconstruction. The standard SIRT method provides a higher-quality reconstruction than the FBP method due to the high levels of noise rejection. The main reason for choosing our method of reconstruction as opposed to, for example, the classical FBP algorithm, was the quality of the reconstructed images. We found that despite being useful (and faster), the FBP approach was inferior to SIRT in image reconstruction quality.

Data correction and image reconstruction using subresolution fluorescent beads as fiducials

For spatial resolution characterization of the LCCT system, we used cells containing 3 to 10 internalized 200-nm-diameter fluorescent polystyrene beads. The bead size was chosen so that one can distinguish between single beads and clusters of two or more beads. Owing to the point source–like fluorescence intensity distribution of the beads, as opposed to the more diffused signal when using fluorescent markers inside the cell, the image processing and reconstruction algorithms outlined in the previous section were suboptimal for achieving quality reconstructions. The registration algorithms were based on the alignment of center of mass of more or less diffusely distributed fluorescence signal inside the cell. In case of sparsely distributed few bright spots representing beads, however, the center of mass approach falls short of performing reliable registration, which results in distorted volumetric reconstructions. To avoid this, we have developed another image processing and reconstruction computational pipeline that is not based on center of mass registration and accounts for the specifics of fluorescent bead signal. We also noticed that rotation of cells containing the dielectric polystyrene beads was associated with more pronounced lateral shift along the axis of rotation as compared with cells that did not have beads inside. It is likely that the dielectric properties of the beads caused local distortions of the electric field, leading to the observed net translation that needs to be corrected computationally.

To precondition the raw projection data for the image reconstruction algorithm, the first step in the image processing was to characterize and correct for nonuniform rotation and rotation axis. Simulations were performed using Matlab (version R2016a, MathWorks Inc.) to assess the effects of a rotation axis translation and in-plane rotation, as well as the more complex case of out-of-plane axis rotations.

In conventional x-ray CT, projection data are often sorted into a "sinogram" format where data acquired with a 1D array of sensors are presented as a function of viewing angle in a 2D image. This ordering of the data shows the change in attenuation for each detector as a function of viewing angle. In the case of LCCT, we considered the direction within a projection that is parallel to the axis of rotation to be the "detector" direction and the perpendicular direction to be the "slice" (analogous to multislice CT) direction (fig. S16). To display sinograms, an MIP was used to reduce the data to two dimensions (fig. S17).

A robust, automated algorithm was developed to detect in-plane perturbations using data acquired with beads. The algorithm is based on tracking the detector sinogram of the various beads first and then using the deviations from the fit to an ideal sine curve to derive a set of measured and ideal locations for each projection. This information was used as input to a rigid body transformation estimate. Finally, this estimate was used to correct each projection with rotation and translations. The algorithm is called "GeoFit" (fig. S18). GeoFit was applied to a data set of a cell containing >3 beads. The sinograms in fig. S19 show

uncorrected versus corrected results, demonstrating a marked improvement of the reconstructed volumetric images of the beads in the cell (fig. S20).

So-called "out-of-plane" errors can be thought of as a change in orientation of the rotation axis with respect to the imaging plane. In contrast to the in-plane errors, which act upon individual projections and can be corrected on a projection-by-projection basis, out-of-plane rotations affect multiple projections and must be derived from a consideration of the 3D object as a whole. The algorithm to characterize and correct these deviations relies on a comparison between measured and computed projections. The computed projections were derived from a 3D reconstruction of a subset that excludes projections to be corrected. The comparison was done as a 2D correlation, which serves as a cost function for a simplex-based optimizer that searches for optimal "elevation" angles. The algorithm is called "FixPP" (fig. S21), and it was validated by applying to simulated Shepp-Logan phantom data with a 10° tilt of the axis of rotation over several projections applied (fig. S22). The left image shows an uncorrected reconstruction; notice the degradation of the smaller dark ellipse and the small bright ellipse as compared with the corrected image (right).

3D image analysis and visualization

Reconstructed 3D images were analyzed, rendered, and visualized using the Amira software (version 5.6.0, FEI). 3D object counting and characterization were performed using ImageJ (version 1.51f, National Institutes of Health; http://imagej.nih.gov/ij).

SUPPLEMENTARY MATERIALS

Supplementary material for this article is available at http://advances.sciencemag.org/cgi/content/full/3/12/e1602580/DC1

fig. S1. Microfabrication steps of the electrocage chip for live-cell rotation.
fig. S2. Determination of the optimal voltage range of the electric field used to rotate live cells.
fig. S3. Cell rotation speed as a function of electric field frequency applied to the microelectrodes of the electrocage.
fig. S4. A live K562 cell incubated with 200-nm fluorescent polystyrene beads.
fig. S5. Photobleaching kinetics of the Hoechst 33342 dye in a live K562 cell.
fig. S6. Confocal micrographs showing enlarged mitochondrial structures in J774A.1 cells after treatment with 8-bromo-cAMP, a mitochondrial fission inhibitor.
fig. S7. A device used to simulate electric field conditions in the electrocage during cell rotation on bulk cell samples for assessing potential stress levels introduced by the electric field.
fig. S8. Testing potential cell stress caused by the exposure to high-frequency electric fields used in the electrocage for cell rotation using the device shown in fig. S7.
fig. S9. Assessing potential changes in cellular morphology as a result of exposure to high-frequency electric fields via imaging.
fig. S10. Imaging system setup and implementation.
fig. S11. A diagram of the overall LCCT system design and control.
fig. S12. Piezo scanning, control, and synchronization time diagrams (green, objective scanning voltage; red, triggering pulse; and yellow, acquisition exposure control waveform).
fig. S13. Comparison of the reconstruction of the various registration methods.
fig. S14. Computational workflow used in the modified SIRT and blind deconvolution SIRT methods of volumetric image reconstruction.
fig. S15. Performance demonstration of four different volumetric reconstruction approaches used in the study.
fig. S16. The principle of sinogram generation.
fig. S17. Examples of detector and slice sinograms generated from simulated projection images of two beads moving in circular, distortion-free trajectories.
fig. S18. Description of the GeoFit algorithm computational pipeline, which estimates and corrects in-plane projection perturbations—Lateral shift and in-plane orientation changes of the rotation axis.
fig. S19. Correction of in-plane perturbations of rotation using the GeoFit algorithm.
fig. S20. Slice of a volumetric image reconstructed using raw/uncorrected data (left) and after correction using the GeoFit algorithm (right).
fig. S21. Pipeline description of the FixPP algorithm to correct out-of-plane perturbations.
fig. S22. Reconstruction of simulated Shepp-Logan data with 10° axis elevation using the FixPP algorithm.
movie S1. Raw PP images of a live human myelogenous leukemia (K562 cell line) cell rotating in the electrocage.
movie S2. Raw PP images of a live K562 cell with internalized 200-nm fluorescent beads rotating in the electrocage.
movie S3. Reconstructed 3D volumetric image (surface rendering) of the K562 cell shown in movie S2.
movie S4. Comparison between the confocal and LCCT imaging modalities.
movie S5. Surface rendering of a reconstructed 3D volumetric image of a live K562 cell with stained nucleus (blue-green) and mitochondria (red-yellow).
movie S6. Nuclear feature segmentation of a reconstructed 3D volumetric image of a live K562 cell.
movie S7. Mitochondrial feature segmentation of a reconstructed 3D volumetric image of the same cell as shown in movie S4.
movie S8. Overlay of nuclear (green) and mitochondrial (red) feature segmentation results and their corresponding MIP renderings shown in movies S4 and S5.
movie S9. MIP and separate slices of the reconstructed 3D volumetric images of mitochondria in the same cell shown in movies S5 to S8.
movie S10. Mitochondrial fluorescence intensity and segmentation results using the Niblack local threshold approach.
movie S11. 3D view of mitochondrial segmentation overlaid with fluorescence intensity (both surface renderings).
movie S12. A representative example of mitochondrial segmentation in 3D illustrated as a small ROI from movie S11.
movie S13. 3D rendering and *Z*-stack of the mitochondrial network in a fixed K562 cell imaged using confocal microscopy.
movie S14. Mitochondrial fluorescence intensity and segmentation results of the cell shown in movie S13.
movie S15. Fluorescence intensity and segmentation results of the nucleoli in a live K562 cell.
movie S16. Maximum intensity renderings of reconstructed 3D images of an untreated (left) and treated (right) J774A.1 cell line (mouse macrophage cell) with the mitochondrial fission inhibitor 8-bromo-cAMP.
movie S17. Surface rendering of a reconstructed 3D image of a live J774A.1 cell.

REFERENCES AND NOTES

1. M. G. Meyer, J. W. Hayenga, T. Neumann, R. Katdare, C. Presley, D. E. Steinhauer, T. M. Bell, C. A. Lancaster, A. C. Nelson, The Cell-CT 3-dimensional cell imaging technology platform enables the detection of lung cancer using the noninvasive LuCED sputum test. *Cancer Cytopathol.* **123**, 512–523, (2015).
2. J. Huisken, J. Swoger, F. Del Bene, J. Wittbrodt, E. H. K. Stelzer, Optical sectioning deep inside live embryos by selective plane illumination microscopy. *Science* **305**, 1007–1009 (2004).
3. P. J. Verveer, J. Swoger, F. Pampaloni, K. Greger, M. Marcello, E. H. K. Stelzer, High-resolution three-dimensional imaging of large specimens with light sheet-based microscopy. *Nat. Methods* **4**, 311–313 (2007).
4. A. Kumar, Y. Wu, R. Christensen, P. Chandris, W. Gandler, E. McCreedy, A. Bokinsky, D. A. Colón-Ramos, Z. Bao, M. McAuliffe, G. Rondeau, H. Shroff, Dual-view plane illumination microscopy for rapid and spatially isotropic imaging. *Nat. Protoc.* **9**, 2555–2573 (2014).
5. H. Zhong Applying superresolution localization-based microscopy to neurons. *Synapse* **69**, 283–294 (2015).
6. R. Weissleder, M. Nahrendorf, Advancing biomedical imaging. *Proc. Natl. Acad. Sci. U.S.A.* **112**, 14424–14428 (2015).
7. N. H. Revelo, S. O. Rizzoli, Application of STED microscopy to cell biology questions. *Methods Mol. Biol.* **1251**, 213–230 (2015).
8. A. M. Colberg-Poley, G. H. Patterson, K. Salka, S. Bhuvanendran, D. Yang, J. K. Jaiswal, Superresolution imaging of viral protein trafficking. *Med. Microbiol. Immunol.* **204**, 449–460 (2015).
9. J. Tønnesen, U. V. Nägerl, Two-color STED imaging of synapses in living brain slices. *Methods Mol. Biol.* **950**, 65–80, (2013).
10. M. Furlan-Magaril, C. Varnai, T. Nagano, P. Fraser, 3D genome architecture from populations to single cells. *Curr. Opin. Genet. Dev.* **31**, 36–41 (2015).
11. R. E. Boulos, G. Drillon, F. Argoul, A. Arneodo, B. Audit, Structural organization of human replication timing domains. *FEBS Lett.* **589**, 2944–2957 (2015).
12. K. S. Wendt, F. G. Grosveld, Transcription in the context of the 3D nucleus. *Curr. Opin. Genet. Dev.* **25**, 62–67 (2014).
13. D. U. Gorkin, D. Leung, B. Ren, The 3D genome in transcriptional regulation and pluripotency. *Cell Stem Cell* **14**, 762–775 (2014).
14. M. Hensel, J. Klingauf, J. Klingauf, Imaging the invisible: Resolving cellular microcompartments by superresolution microscopy techniques. *Biol. Chem.* **394**, 1097–1113 (2013).
15. P. Isermann, J. Lammerding, Nuclear mechanics and mechanotransduction in health and disease. *Curr. Biol.* **23**, R1113–R1121 (2013).

16. J. M. Lucocq, T. M. Mayhew, Y. Schwab, A. M. Steyer, C. Hacker, Systems biology in 3D space—Enter the morphome. *Trends Cell Biol.* **25**, 59–64 (2015).
17. E. Nunez, X.-D. Fu, M. G. Rosenfeld, Nuclear organization in the 3D space of the nucleus—Cause or consequence? *Curr. Opin. Genet. Dev.* **19**, 424–436 (2009).
18. L. Shao, B. Isaac, S. Uzawa, D. A. Agard, J. W. Sedat, M. G. L. Gustafsson, I^5S: Wide-field light microscopy with 100-nm-scale resolution in three dimensions. *Biophys. J.* **94**, 4971–4983 (2008).
19. S. W. Hell, M. Schrader, H. T. M. van der Voort, Far-field fluorescence microscopy with three-dimensional resolution in the 100-nm range. *J. Microsc.* **187**, 1–7 (1997).
20. M. R. Junttila, F. J. de Sauvage, Influence of tumour micro-environment heterogeneity on therapeutic response. *Nature* **501**, 346–354 (2013).
21. J. Massagué, A. C. Obenauf, Metastatic colonization by circulating tumour cells. *Nature* **529**, 298–306 (2016).
22. A. C. Kak, M. Slaney, *Principles of Computerized Tomographic Imaging* (Society for Industrial and Applied Mathematics, 2001).
23. M. Fauver, E. J. Seibel, J. R. Rahn, M. G. Meyer, F. W. Patten, T. Neumann, A. C. Nelson, Three-dimensional imaging of single isolated cell nuclei using optical projection tomography. *Opt. Express* **13**, 4210–4223 (2005).
24. T. Neumann, Q. Miao, J. Yu, M. Fauver, M. Meyer, J. R. Rahn, C. A. Lancaster, E. J. Seibel, A. C. Nelson, Simultaneous 3D imaging of morphology and nanoparticle distribution in single cells with the Cell-CT technology. *Conf. Proc. IEEE Eng. Med. Biol. Soc.* 2008, 379–381 (**2008**).
25. C. B. Müller, J. Enderlein, Image scanning microscopy. *Phys. Rev. Lett.* **104**, 198101 (2010).
26. T. Müller, G. Gradl, S. Howitz, S. Shirley, Th. Schnelle, G. Fuhr, A 3-D microelectrode system for handling and caging single cells and particles. *Biosens. Bioelectron.* **14**, 247–256 (1999).
27. C. Reichle, T. Muller, T. Schnelle, G. Fuhr, Electro-rotation in octopole micro cages. *J. Phys. D Appl. Phys.* **32**, 2128–2135 (1999).
28. B. Cao, L. Kelbauskas, S. Chan, R. M. Shetty, D. Smith, D. R. Meldrum, Rotation of single live mammalian cells using dynamic holographic optical tweezers. *Opt. Lasers Eng.* **92**, 70–75 (2017).
29. R. M. Shetty, J. R. Myers, M. Sreenivasulu, W. Teller, J. Vela, J. Houkal, S.-H. Chao, R. H. Johnson, L. Kelbauskas, H. Wang, D. R. Meldrum, Characterization and comparison of three microfabrication methods to generate out-of-plane microvortices for single cell rotation and 3D imaging. *J. Micromech. Microeng.* **27**, 015004 (2016).
30. B.-C. Chen, W. R. Legant, K. Wang, L. Shao, D. E. Milkie, M. W. Davidson, C. Janetopoulos, X. S. Wu, J. A. Hammer III, Z. Liu, B. P. English, Y. Mimori-Kiyosue, D. P. Romero, A. T. Ritter, J. Lippincott-Schwartz, L. Fritz-Laylin, R. D. Mullins, D. M. Mitchell, J. N. Bembenek, A.-C. Reymann, R. Böhme, S. W. Grill, J. T. Wang, G. Seydoux, U. S. Tulu, D. P. Kiehart, E. Betzig, Lattice light-sheet microscopy: Imaging molecules to embryos at high spatiotemporal resolution. *Science* **346**, 1257998 (2014).
31. Y. C. Wu, P. Wawrzusin, J. Senseney, R. S. Fischer, R. Christensen, A. Santella, A. G. York, P. W. Winter, C. M. Waterman, Z. Bao, D. A. Colón-Ramos, M. McAuliffe, H. Shroff, Spatially isotropic four-dimensional imaging with dual-view plane illumination microscopy. *Nat. Biotechnol.* **31**, 1032–1038 (2013).
32. J. E. Chipuk, E. Ingerman, C. Song, C. Yoo, T. Kuwana, M. J. Kurth, J. T. Shaw, J. E. Hinshaw, D. R. Green, J. Nunnari, Chemical inhibition of the mitochondrial division dynamin reveals its role in Bax/Bak-dependent mitochondrial outer membrane permeabilization. *Dev. Cell* **14**, 193–204 (2008).
33. F. Martínez, M. Kiriakidou, J. F. Strauss III, Structural and functional changes in mitochondria associated with trophoblast differentiation: Methods to isolate enriched preparations of syncytiotrophoblast mitochondria. *Endocrinology* **138**, 2172–2183 (1997).
34. W. Niblack, *An Introduction to Image Processing* (Prentice-Hall International, 1986).
35. R. M. Haralick, K. Shanmuga, I. Dinstein, Textural features for image classification. *IEEE Trans. Syst. Man. Cybern* **Smc-3**, 610–621 (1973).
36. B. Huang, M. Bates, X. Zhuang, Super-resolution fluorescence microscopy. *Annu. Rev. Biochem.* **78**, 993–1016 (2009).
37. M. G. L. Gustafsson, Surpassing the lateral resolution limit by a factor of two using structured illumination microscopy. *J. Microsc.* **198**, 82–87 (2000).
38. M. G. L. Gustafsson, P. Kner, B. B. Chhun, E. R. Griffis, Structured-illumination microscopy of living cells, in *Abstracts of Papers of the American Chemical Society* (American Chemical Society, 2009), vol. 238.
39. M. Tokunaga, N. Imamoto, K. Sakata-Sogawa, Highly inclined thin illumination enables clear single-molecule imaging in cells. *Nat. Methods* **5**, 159–161 (2008).
40. S. Lindquist, The heat-shock response. *Annu. Rev. Biochem.* **55**, 1151–1191 (1986).
41. M. P. Mayer, Gymnastics of molecular chaperones. *Mol. Cell* **39**, 321–331 (2010).
42. J. G. Sørensen, T. N. Kristensen, V. Loeschcke, The evolutionary and ecological role of heat shock proteins. *Ecol. Lett.* **6**, 1025–1037 (2003).
43. A. Cheddad, C. Svensson, J. Sharpe, F. Georgsson, U. Ahlgren, Image processing assisted algorithms for optical projection tomography. *IEEE Trans. Med. Imaging* **31**, 1–15 (2012).
44. G. T. Herman, D. Roberts, L. Axel, Fully three-dimensional reconstruction from data collected on concentric cubes in Fourier space: Implementation and a sample application to MRI. *Phys. Med. Biol.* **37**, 673–687 (1992).

Acknowledgments: We thank M. Bennett for cell culture needs, J. Vela and J. Houkal for help with mechanical engineering of the platform, and V. Nandakumar for the valuable discussions. **Funding:** This work was supported by a grant from the W. M. Keck Foundation (024333-001) to D.R.M. **Author contributions:** L.K. conceived and designed the experiments, co-developed the technological platform and image reconstruction software, performed data analysis and interpretation, and wrote the manuscript. R.S. and B.C. performed data collection and analysis. K.-C.W. and H.W. microfabricated and optimized the electrocage performance. D.S. developed the system control software and optimized the setup performance. S.-H.C. and S.G. built the cell stress instrument and performed stress experiments. B.A. and M.K. developed the image processing and reconstruction software for cell seeding and harvesting. H.G. conceived and performed mitochondrial fusion inhibition experiments using confocal imaging. R.H.J. co-developed the platform and provided daily guidance. D.R.M. provided overall leadership and supervision of the project, participated in all aspects of the technology development and experiments, and critically reviewed the manuscript. **Competing interests:** There are several patent applications and filings related to this work. D.R.M., R.H.J., L.K., B.A., D.S., H.W., S.-H.C., and R.S. are inventors on a U.S. provisional filing 62/302,649 (filed 2 March 2016). B.A., R.H.J., and D.R.M. are inventors on a U.S. provisional filing 62/466,306 (filed 2 March 2017). D.R.M., R.H.J., H.W., L.K., and D.S. are inventors on a U.S. provisional patent application 61/882,117 (filed 25 September 2013). H.W., D.R.M., R.S., L.K., and S.-H.C. are inventors on a U.S. provisional patent application 62/054,839 (filed 24 September 2014). All the other authors declare that they have no competing interests. **Data and materials availability:** All data needed to evaluate the conclusions in the paper are present in the paper and/or the Supplementary Materials. Additional data related to this paper may be requested from the authors.

Submitted 19 October 2017
Accepted 6 November 2017
Published 6 December 2017
10.1126/sciadv.1602580

Citation: L. Kelbauskas, R. Shetty, B. Cao, K.-C. Wang, D. Smith, H. Wang, S.-H. Chao, S. Gangaraju, B. Ashcroft, M. Kritzer, H. Glenn, R. H. Johnson, D. R. Meldrum, Optical computed tomography for spatially isotropic four-dimensional imaging of live single cells. *Sci. Adv.* **3**, e1602580 (2017).

Science Advances

Optical computed tomography for spatially isotropic four-dimensional imaging of live single cells

Laimonas Kelbauskas, Rishabh Shetty, Bin Cao, Kuo-Chen Wang, Dean Smith, Hong Wang, Shi-Hui Chao, Sandhya Gangaraju, Brian Ashcroft, Margaret Kritzer, Honor Glenn, Roger H. Johnson and Deirdre R. Meldrum

Sci Adv **3** (12), e1602580.
DOI: 10.1126/sciadv.1602580